Evaluation of Laminar Mixing in Stirred Tanks using a Discrete Time Particle Mapping Procedure

Albert Harvey III*, David West*, Nicholas Tufillaro
Integrated Solutions Laboratory
HP Laboratories Palo Alto
HPL-1999-56
April, 1999

flow field,
stirred tank,
mixing,
Poincaré map,
advection equation,
mixing efficiency

While much progress has been made in computing the flow field in stirred tanks, the flow field alone does not really give any direct information about a very important characteristic of the design, namely the mixing time. Efficient and accurate computational tools are needed to compute mixing time and to identify isolated mixing regions. In this paper we attempt to address both of these needs by developing a discrete-time model of the flow in a stirred tank based on a numerical approximation of the Poincaré map. We start by computing the 3D flow field. Next we integrate the advection equation for more than 10^4 passive particles through one period of the flow. A mapping is defined between each particle's initial and final radial and axial coordinates, and the elapsed time for each particle trajectory. The time evolution for tracer particles can then be continued for arbitrarily long times by iterating the map. This mapping procedure is demonstrated on four different impeller stirred tank configurations. It is shown that the error in the mapping procedure can be made to be less than the error in the time integration scheme at a significantly reduced computational effort. Furthermore, as a quantitative aid in evaluating the mixing efficiency, we compute a mixing time which is defined as the time needed for a particle to travel a prescribed distance from its starting location.

* The Dow Chemical Company, Plaquemine, LA

Introduction

Stirred tank reactors (STRs) are often used for conducting polymerization reactions in industry. Because of the high viscosity of polymer solutions, it is often impossible to operate the mixer in the turbulent regime. Molecular weight distribution and polymer structure and properties are often adversely effected by incomplete mixing. A good reactor design must exhibit both good macromixing as well as good micromixing. In laminar STR flows the absence of turbulent diffusion restricts transport across streamlines to the relatively slow process of molecular diffusion. The rate of molecular diffusion in highly viscous fluids is exceedingly slow. Thus transport by diffusion is only important over very small length scales or extremely long time scales. Even in nonviscous solutions such as water the mixing time in the laminar flow regime may be as much as 100 times longer than mixing times in fully turbulent flow (Norwood and Metzner, 1960). Therefore fast large-scale blending, or macromixing, is needed in order to reduce segregation to very small length scales, beyond which diffusion can take care of the rest.

Large scale industrial STRs are often built with height to diameter ratios greater than one to avoid excessive power dissipation. Usually such tanks are fitted with multiple impellers on a single shaft in order to improve mixing. Although the mixing in the immediate vicinity of each impeller may be very fast, there is often only very slow transport between adjacent, well mixed zones [Oldshue (1989); Whitton (1993); Baudou *et al.* (1997)]. Most of the flow between adjacent zones travels in a thin film along the shaft and along the walls of the tank. Avoiding this sort of partial segregation between adjacent zones is important in the design of tanks with multiple impellers.

In the past decade, much progress has been made in computing the flow field of STRs, especially in the laminar flow regime, using Computational Fluid Dynamics (CFD). Detailed calculations for the laminar flow in STRs have been performed by Harvey and Rogers (1996) and Harvey *et al.* (1995). These calculations take into account the impeller geometry and require no experimentally obtained data for "impeller boundary conditions." Thus, flow interactions between adjacent impellers can be accurately computed in stirred tanks that are fitted with multiple impellers as presented in Harvey, *et al.* (1997). This computational work suggests that the circulation patterns (in STRs fitted with multiple impellers), and hence possibly mixing performance, is very sensitive to the relative placement and size of adjacent impellers. One of the main motivations of the present work is to develop an

efficient means of assessing the impact of such design variables on mixing performance in stirred vessels.

In previous computational studies of STR flows various methods have been used for flow visualization. Typically, the results of CFD calculations are presented as plots of the velocity vector field in one or more planar slices through the three dimensional field. Sometimes the three dimensional field is spatially averaged and again presented as a vector field in a 2-D section. Occasionally streamlines are computed from two components of the vector field in some 2-D section of the flow located at a specific coordinate of the transverse dimension, neglecting the third (transverse) component of the velocity. Such streamline plots can also be derived from spatial or time averaged data (*e.g.*, Harvey *et al.*, 1997). All of these techniques are attempts to reduce the number of dimensions of a 3-D flow field, for the purpose of visualizing the flow. At best none of these techniques give any direct information about mixing, and at worst they can give completely misleading impressions about the flow. Another commonly used method for analyzing flow fields involves embedding passive tracer particles in the flow and computing their motion within the flow by solving the Lagrangian equation of motion.

One difficulty in studying mixing in laminar STR flows arises from the very long mixing time inherent in laminar flows (which may be of the order of several hundred impeller revolutions). Another difficulty comes from the inherent sensitivity of chaotic trajectories to errors and the rate of propagation of errors in numerical integration schemes. Souvaliotis *et al.* (1995) have examined the effect of three types of errors present in mixing simulations. They show that integration error can grow proportional to the square of the integration time. Consequently even very small errors can quickly grow to the order of the size of the tank. This property imposes serious limitations on the accuracy of particle trajectory calculations and questions remain regarding the usefulness of such calculations for evaluating mixing performance.

Besides avoiding quantitative errors, a useful calculation must not change the qualitative dynamics of the flow. The Hamiltonian nature of 3-D laminar flows results in the formation of invariant (KAM) surfaces which separate the chaotic regions of the flow [see for example Ottino (1989), Aref and El Naschie (1995), and references therein]. KAM tori located above and below the impeller have been observed experimentally in an STR flow (Lamberto *et al.*, 1996). More recently Fountain *et al.* (1998) presented experimental results for a tank

stirred by a rotating disk. Their work revealed some of the detailed structure of the KAM tori using a laser sheet illumination technique. One of the key objectives in the design of STRs is to minimize the number and size of isolated mixing regions, or better, to prevent their existence altogether. Therefore it is essential that such features in the flow are neither created nor destroyed as an artifact of the numerical integration.

In virtually all past computational studies of the STR, mixing performance has been assessed entirely from velocity vector distributions. Although these plots yield valuable information about flow patterns in the vessel they do not give any direct information about mixing. The most rigorous computational analysis of mixing would be to solve a three-dimensional time-dependent scalar transport equation for species concentration in the stirred tank reactor. However the computational effort for such a calculation would be orders of magnitude larger than computing the flow field. Furthermore, a single expensive integration of a scalar transport equation would often be insufficient. To fully analyze mixing performance in a stirred vessel, different initial conditions (feed input locations) should be examined, which would require multiple costly computations. It is a goal of the present work to develop a quantitative method for computing mixing performance which is more computationally tractable than solving the full unsteady scalar transport problem.

In this paper we develop a discrete-time model of the flow, based on a numerical approximation of the "Poincaré map." The map is created by integrating the advection equation for approximately 10^4 particles through one period of the flow. The final r and z coordinates and travel time are recorded for each of the particles at the stopping location. A map is defined between the initial and final coordinates (including time). The time evolution of advected particles is examined by computing the suspension of the map. The long time behavior of a smaller number of particles (36) is examined by computing the suspension of the map for many periods of the flow. The results are conveniently displayed as a Poincaré section of the flow, which reduces the dimensions of the problem by one. A mixing time is defined based on an arbitrary measure of mixing. Results from the discrete-time model are compared with numerical integration for four tank geometries. Previous results have derived mixing properties from direct integration of particle trajectories, which is computationally very expensive. Our approach reveals the same global mixing properties of the flow in a much more computationally efficient manner. We conclude with a brief assessment of the numerical accuracy of the method compared with direct integration.

The mapping can be applied to different multiple impeller reactor configurations to determine the location of the invariant surfaces and KAM tori which act a barriers to global mixing. Knowledge of these issues will facilitate the design of improved stirred tanks. Internal impeller configurations can be adjusted to facilitate flow between adjacent impellers, and inlet and exit feed locations can be positioned for optimal mixing conditions.

Discrete Time Model

In this section we describe a method for creating a discrete time model of the advection of passive particles, and derive estimates of the mixing effectiveness, including the mixing time.

We demonstrate the construction of the map using examples computed for a three dimensional, laminar flow field in an impeller stirred vessel for a number of different internals configurations (see Fig. 3). Additional details of the geometry and flow are presented in the next section. In these flow examples a large number of particle trajectories (10011 and 39621 for the coarse and fine grids, respectively) are computed for a period of time equal to the time required for 500 *relative* revolutions of the impeller. What we mean by relative revolution is described next.

To create the discrete-time map we start with an evenly spaced grid of initial particle locations at time $t = t_o$, and we compute each particles' motion (by integrating the advection equation) through one complete period of the flow. During one period of the flow, the impeller makes one complete revolution *relative* to each particle. Thus the distance and time traveled will, in general, be different for each particle. This procedure is graphically illustrated in Fig. 1. Figure 1*a* shows the initial orientation of the impeller and the ith particle at time $t = t_o$. The impeller is rotating at a speed of Ω and the particle is, at the initial instant, moving with velocity v_p. Since the highest velocity in the tank is the tip velocity, the particle velocity will never be as high as the impeller speed. When viewed from an Eulerian frame of reference, the particles will appear to circulate around the circumference of the tank in the same direction as the impeller, as illustrated in Figs. 1*a*–*e*. The particle motion will however, lag the motion of the impeller and the impeller will rotate *at least* one complete revolution (relative to the tank) before moving past the particle again. At this point the impeller is once again at its initial θ-orientation relative to the ith particle. We cease integration of each particle trajectory when each has

traveled through one period of the flow; *i.e.*, when the relative orientation of the particle and the impeller return to their initial θ-orientation. This stopping condition is found by monitoring the angle ϕ between each particle and a reference position, R, attached to the rotating frame. When $\phi = 2\pi$ for the ith particle we stop the integration procedure for that particle and note its total time as $(\delta t)_i$. The hyperplane containing the particles at their final location defines a *Poincaré section* of the flow. A *relative impeller revolution*, so defined, will hereafter be referred to as a single period of the flow.

It should be noted here that the same basic procedure for constructing the Poincaré section can be applied to tanks with wall baffles. However, for a baffled tank the implementation is not as straightforward since the flow period is different. The appropriate stopping condition for the integration is when a particle has returned to the same relative angular position with respect to both the impeller and a reference point on the wall of the tank (e.g., a baffle) simultaneously (which is one period of the flow).

A second order Adams multistep method is used for the time integration of the particles. The error associated with this scheme is discussed in a later section. Once the initial integration step is complete, the position vector of each particle at the $\phi = 0$ and $\phi = 2\pi$ hyperplanes is known. Next we seek a formal relationship which maps the set of initial coordinates for each particle, $\mathbf{x}_i^o$, (at $\phi = 0$) to the set of final coordinates for each particle, $\mathbf{x}_i^1$, (at $\phi = 2\pi$). This mapping can be constructed as follows:

$$\mathbf{x}_i^{n+1} = A_i \mathbf{x}_i^n \tag{1}$$

This expression maps the position vector, $\mathbf{x}_i^{n+1}$ of the ith particle at the $n+1$th period of the flow (at $\phi = 2(n+1)\pi$) to the particles' position vector at the previous or nth revolution, $\mathbf{x}_i^n$ (at $\phi = 2n\pi$). The coefficient matrix, A_i, is a diagonal matrix whose off diagonals are zero and the diagonal elements are found after integrating the particles for the first period of the flow. An attractive feature of the mapping is that it reduces the dimension of the three-dimensional system by one. Therefore the vector $\mathbf{x}_i$ contains only the radial coordinate $r_i = \sqrt{x_i^2 + y_i^2}$ and the axial coordinate z_i. Thus Eq. (1) can be rewritten as:

$$r_i^{n+1} = f_r(r_i^n, z_i^n); \qquad z_i^{n+1} = f_z(r_i^n, z_i^n)$$

The map defined by Eq. (1) is continuously and infinitely differentiable with respect to the scalar components of $\mathbf{x}$. The mapping is also invertible and one-to-one and the matrix

A_i can be made to have only positive diagonal elements by a suitable choice of the origin of the coordinate system. Therefore the Jacobian of Eq. (1) is everywhere positive, so the map is orientation preserving. The two diagonal elements of the coefficient matrix A_i are computed as follows

$$A_i = \begin{pmatrix} r_i^1/r_i^o \\ z_i^1/z_i^o \end{pmatrix}$$

where (r_i^o, z_i^o) is the initial position of the ith particle and (r_i^1, z_i^1) is the ending position vector of the particle.

To keep track of time in a common frame of reference, the time needed for the impeller to become re-aligned with the ith particle is denoted as $(\delta t)_i$ and; during iteration of the map of Eqs. (1), the total age of each particle is accounted for by summing the time required for the motion of each iterate of the map.

The mapping procedure can be best explained through the use of Fig. 2 in which the particle P is followed through the first few iterations of the discrete mapping. In this figure, a section of the initial uniform grid of particles (black dots) is shown together with a small section of the final grid point locations (cross-hatched region). Equation (1) is applied to the particle with initial location denoted P_0 in Fig. 2 resulting in its movement to point P_n illustrated by the dotted line. A difficulty now arises due to the fact that the mapping is defined only at a discrete number of locations (black dots) and, unless we use an infinite number of particles, we can never expect a particle to land precisely at a location where the mapping is defined. The point P_n of Fig. 2 is one such point whose trajectory from iteration n to iteration $n+1$ (shown by the dash-dot line) is unknown. Interpolation of the discrete mapping involves finding a unique point P_{n+1} for points like that of point P_n which lie off the discrete mapping.

The next step is to find the index i, j of the point in the discrete mapping which is closest to the current particle position P_n. A simple search algorithm can be constructed to find point 1 which is closest to P_n and also the points 2–4, together which makeup P_n's four closest neighbors. From the mapping we know that points 1–4 map to the points $1'$–$4'$.

At this point, the simplest way to approximate P_{n+1} would be to use the nearest neighbor and map all points that are closest to the point 1 (which would fall into the shaded square of Fig. 2) to the point $1'$. Such a map is not one-to-one, and therefore unacceptable.

The next simplest interpolation procedure would be to use a bilinear interpolation to

determine P_{n+1} based on the previously found surrounding known values of the discrete mapping (points 1–4). Coefficients Δ_i and Δ_j are found, based on the initial discrete grid points 1–4 in the following manner:

$$\begin{aligned} \mathbf{x}_P = \mathbf{x}_1 + (\mathbf{x}_2 - \mathbf{x}_1)\Delta_i + (\mathbf{x}_3 - \mathbf{x}_1)\Delta_j \\ + (\mathbf{x}_4 - \mathbf{x}_3 - \mathbf{x}_2 + \mathbf{x}_1)\Delta_i\Delta_j \end{aligned} \tag{2}$$

Where $\mathbf{x}_P$ is the position vector of the point P_n of Fig. 2 for which the discrete mapping is to be interpolated. Equations (2) consists of two equations for the unknown coefficients Δ_i and Δ_j. As $\mathbf{x}_P \to \mathbf{x}_1$, then Δ_i and Δ_j tend to zero as required. Similarly, Δ_i and Δ_j both tend to unity as $\mathbf{x}_P \to \mathbf{x}_4$. These coefficients Δ_i and Δ_j are then used to determine the position P_{n+1} from the known mappings of the surrounding points

$$\begin{aligned} \mathbf{x}_{P_{n+1}} = \mathbf{x}'_1 + (\mathbf{x}'_2 - \mathbf{x}'_1)\Delta_i + (\mathbf{x}'_3 - \mathbf{x}'_1)\Delta_j \\ + (\mathbf{x}'_4 - \mathbf{x}'_3 - \mathbf{x}'_2 + \mathbf{x}'_1)\Delta_i\Delta_j \end{aligned} \tag{3}$$

Using this technique, each point in the n-th plane is mapped onto a unique point in the n+1th hyperplane at $\phi = 2\pi n$, so the map is both onto and one-to-one.

If δt_1 represents the time required for a particle to move from point 1 to $1'$ in Fig. 2 and δt_2, δt_3 and δt_4 represent analogous times for points 2, 3 and 4, then the time required for a particle at P_n to move to P_{n+1} can be found using the coefficients Δ_i and Δ_j and an expression similar to Eq. (3).

A bi-cubic interpolation procedure was also performed to study the effect of using higher order interpolation on the performance of the mapping. A sixteen point stencil of points surrounding the point P_n of Fig. 2 was used in this technique. Cubic splines were fit in one direction and then in the other spatial dimension. The stencil was centered around the point P_n except near boundaries of the domain, in which case centering was not possible.

To study the effect of the order of the interpolation on the mapping performance, both the bi-linear interpolation described above and the bi-cubic interpolation is used on each of 4 different stirred tank configurations. For the bi-cubic interpolation, 2 different grid densities are employed. These results are presented in the next sections.

Computational Results

In order to use the particle mapping procedure described in the previous section, the three-dimensional velocity field in a stirred tank is required for the integration of the motion

of the particles for the first flow period. Due to spatial limitations of the present paper, and since the solution procedure for the velocity field is adequately documented in the literature, a full description of the flow solution is not included. Details of these techniques as well as validation of the method with experimental Laser Doppler Velocimetry (LDV) data for laminar flow in impeller stirred vessels and the numerical methods used in the solution of the incompressible Navier-Stokes equations can be found in Harvey *et al.* (1995, 1997); Harvey and Rogers (1996) and references therein.

Vessel Geometry and Operating Conditions

The mapping procedure is demonstrated on the four different stirred vessel geometries illustrated in Figs. 3. In each of these figures the computational grid for all solid surfaces in the domain are displayed. The case 1 and 2 reactor configurations contain three impellers while the other two cases contain four impellers. Case 3 contains an impeller configuration which, starting from the top, contains successively larger impellers and, except for the absence of baffles, is geometrically similar to case 1 in Harvey *et al.* (1997). Table 1 contains the position and size information for each impeller in all four cases. In this table and in the discussions to follow impeller 1 is the impeller closest to the bottom of the tank. Reference to a particular impeller will often be shortened to I_1 and I_2, etc.

The tank diameter, D, is 3.66 m with a total fill height, T, of 4.66 m. The diameter of the largest impeller, $d = 2.2$ m for each case (see Table 1); the impeller rotational speed was 40 rpm ($N = 0.667$ rev/s); fluid kinematic viscosity was 0.0322 m^2/s and the Reynolds number Re$= d^2N/\nu = 100$. This represents typical blending conditions of high viscosity type materials.

Cross-flow Streamlines/Velocity Vectors

Velocity vectors and streamlines are frequently used to visualize fluid flows. The velocity vectors of Figs. 4 are time-averaged (Harvey and Rogers 1996). Cross-flow streamlines are lines drawn tangent to the time-averaged cross-flow velocity vectors in a θ-plane (see Figs. 5). One should be very careful interpreting figures such as Figs. 4 and 5, because they only show data in a two-dimensional cross-section of a flow that is actually three dimensional. When examining plots like Fig. 5 there is a strong tendency for one to *perceive* that the streamlines are closed. With the possible exception of a very few (corresponding to KAM

tori), the lines are not closed. The cross-flow streamlines are relatively short segments of curves which approximate cross sections of the invariant manifolds of the flow. In the real three-dimensional flow, fluid elements may be convected across some of these apparent streamlines in other θ-planes. Thus pictures such as Figs. 4 and 5 tend to suggest barriers in the flow which do not really exist in three dimensions, or in the Lagrangian view of the flow.

The main utility of plots like Figs. 4 and 5 is that they give a qualitative picture of the geometry of the flow and allow one to quickly spot differences that may arise from very subtle changes in tank design. Thus differences in the number and location of hyperbolic and elliptic cycles in the flow are evident by comparing Figs. 4*a*–*d*, and likewise Figs. 5*a*–*d*. For example, in Fig. 5*a* there appears to be five elliptic cycles in the flow, while there are only two in Fig. 5*c*. Similarly, Figure 4*d* suggests the flow for the case 4 configuration has four relatively large elliptic cycles; the first two are located near the tips of the top two impellers, and there are two located near the tip of the third impeller. Two more elliptic cycles, smaller in size, are visible near the impeller shaft in Fig. 4*d*. Qualitative geometric characteristics such as these may be very important in determining the overall mixing performance of a given flow. However, choosing the best reactor configuration from these results alone would be difficult, if not dangerous. Information about the geometry of the flow alone does not give the quantitative measures of mixing performance that we seek in the present work. Perhaps in the future when more is understood about mixing in stirred tanks it will be possible for one to screen designs by simply looking at the geometry of flows as revealed by plots of vector fields and cross-flow streamlines. The results of the next section will illustrate additional features of the flow that are revealed more accurately than is possible using cross-sections of the velocity field and streamlines.

Poincaré Sections

Figures 6*a*–*d* show Poincaré sections in the $\phi = 0$ surface for both direct integration of only 36 particles (Fig. 6*a*) and the mapping procedure using various grid densities and interpolating schemes (Figs. 6*b*–*d*) for the case 1 vessel configuration. For Fig. 6*a*, direct integration was carried out for only 36 particles, the starting location of each is denoted by the large symbols. Each of the 36 trajectories of Fig. 6*a* was carried out for 500 periods of the flow. For Figs. 6*b*–*d*, the particles (10011 for Figs. 6*b*,*c* and 39621 for Fig. 6*d*)

were integrated for only one relative revolution (flow period); the mapping procedure was then applied for the remaining 500 flow periods. The initial particle locations for the 36 particles shown in Figs. 6*a*–*d* (denoted by the large symbols) are identical.

Figs. 6*b* and 6*c* show the performance of the mapping using bi-linear and bi-cubic interpolation, respectively. Fig. 6*d* shows the mapping using the third order interpolation and a grid of particles which is double the size of the one used in 6*b* and 6*c*. Very good agreement between the integration and mapping procedure is observed for all three mappings. The "empty" spaces in Figs. 6*a*–*d* are present because a relatively small number of particles (36) were used to make the figures. Some regions of the tank are separated from others by KAM surfaces. Segregated regions show up as empty subspaces in the Poincaré sections if none of the tracer particles happened to have initial coordinates located within these regions. It is very important that no attracting or repelling *objects* are created as an artifact of error, either in the integration or the map. The existence of such features are clearly inconsistent with the conservative nature of the flow.

Figs. 7, 8 and 9 show the same sequence of mapping results for cases 2, 3 and 4, respectively. Mixing in all these cases is significantly improved over case 1. Particle motion appears more chaotic near the top of the vessel. The partially segregated region at the top of the vessel in case 1 is not present in cases 2–4. The mapping and integration results look remarkably similar for cases 1–3. A large segregated torus exists just below I_2 at the tip for all cases. The smaller torus shaped regions located just above the larger tori in Figs. 7 and 8 does not appear to be as well defined, if present at all, in Fig. 9. The locations of these regions as predicted by the mapping compares well with that of the integration. For case 2 (Figs. 7), a small torus is present at the tip of I_3.

For case 4 using bi-linear interpolation and the coarse grid (Fig. 3*b*), the results obtained with the mapping procedure are not good. Most of the particle motion has collapsed into regions near the impeller blade tips. In the CFD computation for the velocity field, the divergence of the velocity was reduced to a level of 10^{-3} for case 4. In cases 1–3 the divergence was reduced to levels below 10^{-4}, a full order of magnitude lower. A history of the magnitude of the divergence of the velocity versus iteration count in the CFD calculation for each case is plotted in Fig. 10. Probably the poor performance of the lower order mapping solution for case 4 is due to the higher levels of divergence which remained in the velocity field.

Figures 6–9 resolve most of the important structure present in the flow utilizing a very small fraction of the actual dataset generated by the mapping procedure (only 36 out of 39621 particles were used for the fine grids). Figs. 6–9 would not be intelligible if all the particles were shown. In the next sections, techniques which measure mixing performance are presented which make use of the entire dataset.

Particle Separation Distance

Figures 11 show the results obtained with the discrete-time map using the fine grid (141×281) of particles and bi-cubic interpolation. The map was iterated for 500 flow periods. In Fig. 11 each point in the plane is colored according to the maximum distance, $(\Delta s)_{max}$, that the particle (starting from that point) moved in the θ-plane. The maximum separation distance is defined as the maximum separation distance between any two points on the trajectory, and the distance is normalized by the tank height.

Regions colored magenta indicate regions where fluid is convected large distances and can be associated with good mixing. Blue regions indicate regions where fluid convection is low and are associated with trapped or isolated zones in the reactor. Figures 11 portray a well resolved picture of the locations of the poorly mixed regions in each reactor design. Note that in all of the cases, the bottom portion of the reactor is fairly isolated from the upper portion of the reactor. KAM surfaces appear as discontinuities in the color scheme of the plots of Figs. 11. For case 1 (Fig. 11*a*), mixing from the liquid level surface is poor. The figure also shows the location of 2 distinct isolated regions near the tips of the top two impellers in the reactor. Fig. 11*b* (case 2) shows 3 isolated tori which are colored blue. Mixing near the surface of the tank has noticeably improved over case 1. Case 3 (Fig. 11*c*) illustrates good mixing compared with the other cases. There are no tori present for the top two impellers. The top impellers have been sized so that very little flow separation occurs between I_2 and I_3 and between I_3 and I_4.

For optimal mixing we would like a fluid element at each point in the reactor to visit every other point in the reactor. This would mean that $(\Delta s)_{max}$ for each point would be unity. Every point contained inside a chaotic region of the reactor will visit every other point inside that chaotic region. A way to improve mixing is to make the chaotic regions large; the optimal being a single chaotic "sea" that encompasses the entire vessel.

Mixing Time Calculations

If the value of $(\Delta s)_{max}$ is integrated over the tank volume V as follows:

$$(\widetilde{\Delta s})_{max} = \frac{1}{V}\int_v (\Delta s)_{max} dV$$

thus, a purely quantitative measure of mixing is obtained. The values of $(\widetilde{\Delta s})_{max}$ are tabulated in Table 2 for each case. The best performing mixer is case 3. These results show the sensitivity of the mapping results to grid refinement and order of the interpolation. The results using the higher order interpolation are less sensitive to grid refinement than the lower order interpolation results.

If an integral scale, Δs, is assigned (arbitrarily) to indicate a certain level or degree of "mixedness" say $\Delta s = R$ (vessel radius), then the time required for the particles to reach this degree of separation from their initial conditions can be calculated. Figures 12 show a map of the mixing time for each case. Blue regions indicate fast mixing; red regions indicate relatively slow mixing. In Figs. 13, the fraction of the tank volume which has reached this level of particle separation is plotted as a function of time. The reference time, t_{ref} is the time required for the impeller to make 500 revolutions. The results for mixing time presented in Figs. 13 for cases 1–3 are relatively insensitive to the mapping resolution. However, the results for case 4, in which the velocity divergence is an order of magnitude higher than the other cases, some sensitivity to the mapping resolution is evident. For the coarse grid (71×141) with linear interpolation, the fraction of the tank which is mixed levels off to about 0.77. For the coarse grid with cubic interpolation the tank volume fraction mixed at long times is about 0.95.

Comparing the differences between Figs. 13*a* and 13*b* with the differences in Figs. 13*c* and 13*d* one can see that, using the higher order interpolation, the mapping is less sensitive to the grid density than when using linear interpolation. These differences in sensitivity to grid density and interpolation order is also evident by comparing the numbers in Table 2. It is evident that the performance of the mapping is more easily and efficiently improved by increasing the order of the interpolation than by simply increasing the density of the particles involved.

Estimation of Error

Since the three-dimensional velocity field is obtained numerically, knowledge of flow field variables is available only at discrete locations.

In order to obtain a continuous particle path in the flow, interpolation of the discrete velocity field is required. This procedure will inevitably increase the amount of divergence in the flow to some level above that amount illustrated in Fig. 10 and will ultimately adversely affect the final results of the mapping.

First we evaluate the error introduced by the time integration procedure. As mentioned earlier, a second order Adams multistep method is used for the time integration of the particles. For all computations, a time step of $\Delta t = 0.0015$ seconds was used. Souvaliotis *et al.* (1995) show that the *global* error associated with a time integration scheme is proportional to the square of time. Using their notation we write the global error in the particle position at the kth time integration step as:

$$|\Delta x^{(1)}| = |x_N^{(1)} - x^{(1)}| = A\Delta t^{m-1} t^2 \tag{4}$$

where $x^{(1)}$ is the exact particle position, $x_N^{(1)}$ is the numerical approximation, Δt is the step size of the time integration, m is the order of accuracy, t is the time and A is a constant. For flow between concentric cylinders, they show that the constant of proportionality in this error term $A \leq 0.001$ for all $t \leq 100$. If we assume the error is the same for the present stirred tank computations, then direct integration of a particle for one relative impeller revolution ($t \approx 1\ s$), results in an error in the position vector, $|\Delta x^{(1)}| \leq 10^{-6}\ m$. However, for integration of a particle for 500 impeller revolutions ($\approx 750\ s$), the accumulated error is about $0.84\ m$, which is clearly unacceptable and of the same order as the largest scale of the system. However, there is no reason to believe that the constant of proportionality, A, for the present application is, in any way, comparable to that for flow between concentric cylinders.

Now we consider the global error in the present mapping procedure. For the map, Eq. (4) represents the total error accumulated during the initial integration of the particle (after the first flow period). In additional to this we expect error to accumulate with successive iterations of the map.

The *local* error associated with each flow period (iteration of the map) is $|\Delta x_N^{(i)}| = O(\delta x^p)$, where δx is the mapping mesh size and p is the order of accuracy of the spatial interpolation scheme. Using an analysis similar to that in Souvaliotis *et al.* (1995), the

total error at the kth flow period using the mapping is:

$$\begin{aligned} |\Delta x^{(k)}| &= |\Delta x^{(1)}| + \left| \sum_{i=2}^{k} F^{(i \to k)} \cdot \Delta x_N^{(i)} \right| \\ &\leq |\Delta x^{(1)}| + \sum_{i=2}^{k} |F^{(i \to k)} \cdot \Delta x_N^{(i)}| \\ &\approx |\Delta x^{(1)}| + \sum_{i=2}^{k} B_i (k-i) \delta t_i |\Delta x_N^{(i)}| \end{aligned} \tag{5}$$

where, as in Souvaliotis (1995), B_i depends on the flow-field, and $F^{(i \to j)}$ refers to the exact mapping and δt_i is the time associated with the ith iteration of the map. Substitution of Eq. (4) into Eq. (5) and also letting $B = \max(B_i)$, $\delta t = \max(\delta t_i)$, $|\Delta x_N| = \max|\Delta x_N^{(i)}|$ and assuming strict equality, an expression for total error at the kth iteration of the map is obtained

$$\begin{aligned} |\Delta x^{(k)}| &\leq A \Delta t^{m-1} t_1^2 + B |\Delta x_N| \delta t \frac{k(k-2)}{2} \\ &< A \Delta t^{m-1} t_1^2 + \frac{B}{2} \frac{|\Delta x_N|}{\delta t} (k \delta t)^2 \end{aligned} \tag{6}$$

where t_1 is the time after the first period of the flow. Substituting $|\Delta x_N| = B_N (\delta x)^p$, we can write

$$\begin{aligned} |\Delta x^{(k)}| &< A \Delta t^{m-1} t_1^2 + \frac{B B_N}{2} \frac{(\delta x)^p}{\delta t} t^2 \\ &< A \Delta t^{m-1} t_1^2 + C \frac{(\delta x)^p}{\delta t} t^2 \end{aligned} \tag{7}$$

The numerical integration results from the first relative revolution of the impeller *are used at each iterate of the map.* In order that the error in the map be less than that due to direct integration we must have

$$\frac{|\Delta x^{(k)}|_m}{|\Delta x^{(k)}|_i} = \left(\frac{t_1}{t} \right)^2 + \frac{C}{A} \frac{(\delta x)^p}{\delta t \Delta t^{m-1}} < 1$$

or for large times, t

$$\frac{C}{A} \frac{(\delta x)^p}{\delta t} \frac{1}{\Delta t^{m-1}} < 1 \tag{8}$$

In the present results, the time integration step-size, $\Delta t = 0.0015$ for all calculations, and $k = 500$ iterations corresponds to approximately $t = 750$ seconds. Assuming the constants A and C are equal, Eq. (8) yields 11.5, 0.0078 and 0.00098 for the coarse grid with bi-linear interpolation, the coarse grid with bi-cubic interpolation and the fine grid with bi-cubic, respectively.

There is no reason to assume that the constants of proportionality, A and C, are equal. In fact, to properly account for the vast difference in time scales between one integration step and one iteration of the map, the assumption that $A\Delta t = C\delta t$ would seem more appropriate. If this is true then we can see that the error in fine grid mapping with bi-cubic interpolation is of the same order as the error in the time integration. It is worth pointing out, with reference to Eq. (8), that the mapping can always be made more accurate than direct time integration with proper selection of the interpolation scheme and particle grid resolution, δx. On an equal error basis, the mapping requires much less effort.

Computational Requirements

Use of the mapping procedure can result in significant savings in computational effort. Integration of the motion for just the 36 particles shown in Figs. 6*a*–9*a* for 500 relative revolutions of the impeller required approximately 22 hours of CPU time on a 500Mhz DEC Alphastation. At this rate it is easy to see that integration of a number of particles equal to the coarse grid density (10011) for a comparable length of time would be expensive to say the least. Direct integration of a population equal to the fine grid (39621) would be virtually impossible using the current step-size. The mapping procedure took approximately 1.4 hours of CPU time for the coarse grid and 5 hours for the fine grid on the same computer.

Concluding Remarks

A particle mapping procedure for laminar flow in stirred vessels has been developed. The technique involves direct integration of the motion of a uniform grid of particles for one complete revolution of the impeller relative to each particle. Subsequent particle motion is then obtained by the iteration of an algebraic map. Using this technique the motion of tens of thousands of particles can be computed efficiently in stirred tank vessels for time scales on the order of the actual mixing time. Direct integration of a comparable number of particles for this length of time would possibly take several orders of magnitude more computational time than that required by the mapping. We have shown that the mapping procedure can be made more accurate than direct particle integration at a fraction of the cost.

A mixing time was defined based on the time required for a particle to achieve some arbitrary separation distance. This mixing time calculation can be used to compare different

stirred tank configurations and to assess the effect of impeller speed.

The computed Poincaré sections reveal details of the flow, such as isolated mixing regions, which are not apparent in the velocity vector field. We have shown that the relative impeller size and spacing can be altered so as to increase the size of the active mixing regions. With knowledge of the locations of isolated mixing regions, improved feed input and output locations can be identified.

Acknowledgements

The authors would like to thank Dr. John Guckenheimer, professor of mathematics and of theoretical and applied mechanics at Cornell University for his valuable suggestions and comments. We would also like to thank the reviewers of the manuscript for their valuable suggestions.

Literature Cited

Aref, H., M. S. El Naschie, (1995) *Chaos Applied to Fluid Mixing.*, Elsevier Science Ltd., Oxford, U.K.

Baudou, C., C. Xuereb and J. Bertrand (1997) "3-D Hydrodynamics Generated in a Stirred Vessel by a Multiple-propeller System." *Can. J. Chem. Eng.*, **75**, 653–662.

Fountain, G.O., D.V. Khakhar and J.M. Ottino, (1998) "Visualization of Three-Dimensional Chaos." *Science*, **181**, 683–686.

Harvey, A.D., S.P. Wood, and D.E. Leng, (1997) "Experimental and Computational Study of Multiple Impeller Flows." *Chem. Engng Sci.*, **52**, (May) 1479–1491.

Harvey, A.D., and S.E. Rogers, (1996) "Steady and Unsteady Computation of Impeller Stirred Reactors." *AIChE J.*, **42**, (October), 2701–2712.

Harvey, A.D., C.K. Lee, and S.E. Rogers, (1995) "Steady-State Modeling and Experimental Measurement of a Baffled Impeller Stirred Tank." *AIChE J.*, **41**, (October), 2177–2186.

Lamberto, D.J., F.J. Muzzio and P.D. Swanson, (1996) "Using Time-Dependent RPM to Enhance Mixing in Stirred Vessels." *Chem. Engng. Sci.*, **51**, 733–741.

Norwood K.W., and A.B. Metzner, (1960) "Flow Patterns and Mixing Rates in Agitated Vessels." *AIChE J.*, **6**, 432–437.

Oldshue, J.Y., (1989) "Fluid Mixing in 1989." *Chem. Engng.*, (May), 33.

Ottino, J.M., (1989) *The Kinematics of Mixing: stretching, chaos and transport.* Cambridge Press.

Souvaliotis, A., S.C. Jana and J.M. Ottino, (1995) "Potentialities and Limitations of Mixing Simulations." *AIChE J.*, **41**, 1605–1621.

Whitton, M.J., (1993) "Gas Liquid Mixing in Tall Vessels Fitted with Multiple Impellers." Ph.D. Thesis, Cranfield Institute of Technology.

Table 1: Impeller placement characteristics.

Case #	Impeller	Dia. $[m]$	Height $[m]$
1	I_1 (FBT)	1.1	0.60
	I_2 (PBT)	2.2	2.26
	I_3 (PBT)	1.7	3.94
2	I_1 (FBT)	1.0	0.60
	I_2 (PBT)	2.2	2.10
	I_3 (PBT)	1.7	3.60
3	I_1 (FBT)	1.0	0.60
	I_2 (PBT)	2.2	1.60
	I_3 (PBT)	1.7	2.60
	I_4 (PBT)	1.2	3.60
4	I_1 (FBT)	1.1	0.60
	I_2 (PBT)	2.2	1.60
	I_3 (PBT)	2.2	2.60
	I_4 (PBT)	2.2	3.60

Table 2: Mixing time measure: $\frac{1}{V}\int_V (\Delta s)_{max}\, dV$

Case #	71×141 $O(1)$	241×281 $O(1)$	71×141 $O(3)$	141×281 $O(3)$
1	0.5977	0.6327	0.6590	0.6508
2	0.8937	0.9061	0.9168	0.9065
3	0.8863	0.9212	0.9300	0.9303
4	0.6521	0.8151	0.9064	0.8974

Table 1: Impeller placement characteristics.

Table 2: Mixing time measure: $\frac{1}{V}\int_V (\Delta s)_{max} dV$

Fig. 1: Relative motion of particle and impeller.

Fig. 2: Poincaré mapping interpolation procedure.

Fig. 3: Geometry and surface grid for cases 1–4.

Fig. 4*a–d*: Time-averaged velocity vectors for cases 1–4.

Fig. 5*a–d*: Cross-flow streamlines for cases 1–4.

Fig. 6*a–d*: Poincaré maps for case 1. (*a*) Integration; (*b*) coarse grid, bi-linear mapping interpolation; (*c*) coarse grid, bi-cubic interpolation; (*d*) fine grid, bi-cubic interpolation.

Fig. 7*a–d*: Poincaré maps for case 2. (*a*) Integration; (*b*) coarse grid, bi-linear mapping interpolation; (*c*) coarse grid, bi-cubic interpolation; (*d*) fine grid, bi-cubic interpolation.

Fig. 8*a–d*: Poincaré maps for case 3. (*a*) Integration; (*b*) coarse grid, bi-linear mapping interpolation; (*c*) coarse grid, bi-cubic interpolation; (*d*) fine grid, bi-cubic interpolation.

Fig. 9*a–d*: Poincaré maps for case 4. (*a*) Integration; (*b*) coarse grid, bi-linear mapping interpolation; (*c*) coarse grid, bi-cubic interpolation; (*d*) fine grid, bi-cubic interpolation.

Fig. 10: Plot of the history of the divergence of the velocity field for the CFD calculations (cases 1–4).

Fig. 11*a–d*: $(\Delta s)_{max}$ as a function of position in the vessel (cases 1–4).

Fig. 12*a–d*: Time to achieve $(\Delta s)_{max}$ as a function of position in the vessel (cases 1–4).

Fig. 13*a–d*: Tank volume fraction with $\Delta s \geq (\Delta s)_{max}$ vs. time for the 4 different mappings.

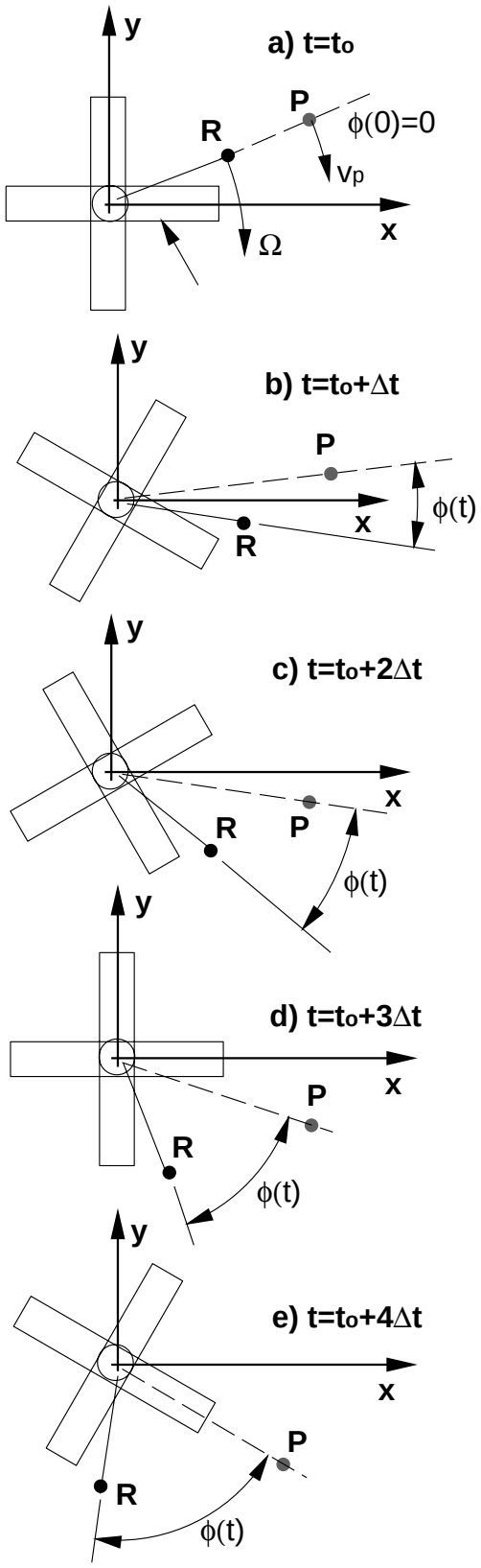

Fig. 1: Relative motion of particle and impeller.

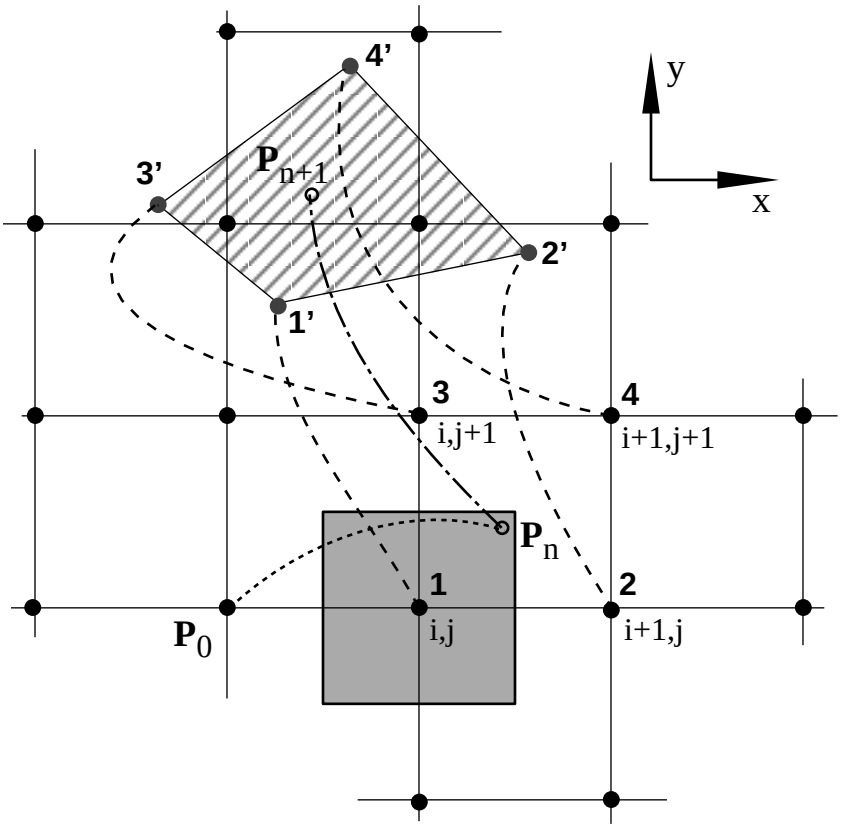

Fig. 2: Poincaré mapping interpolation procedure.

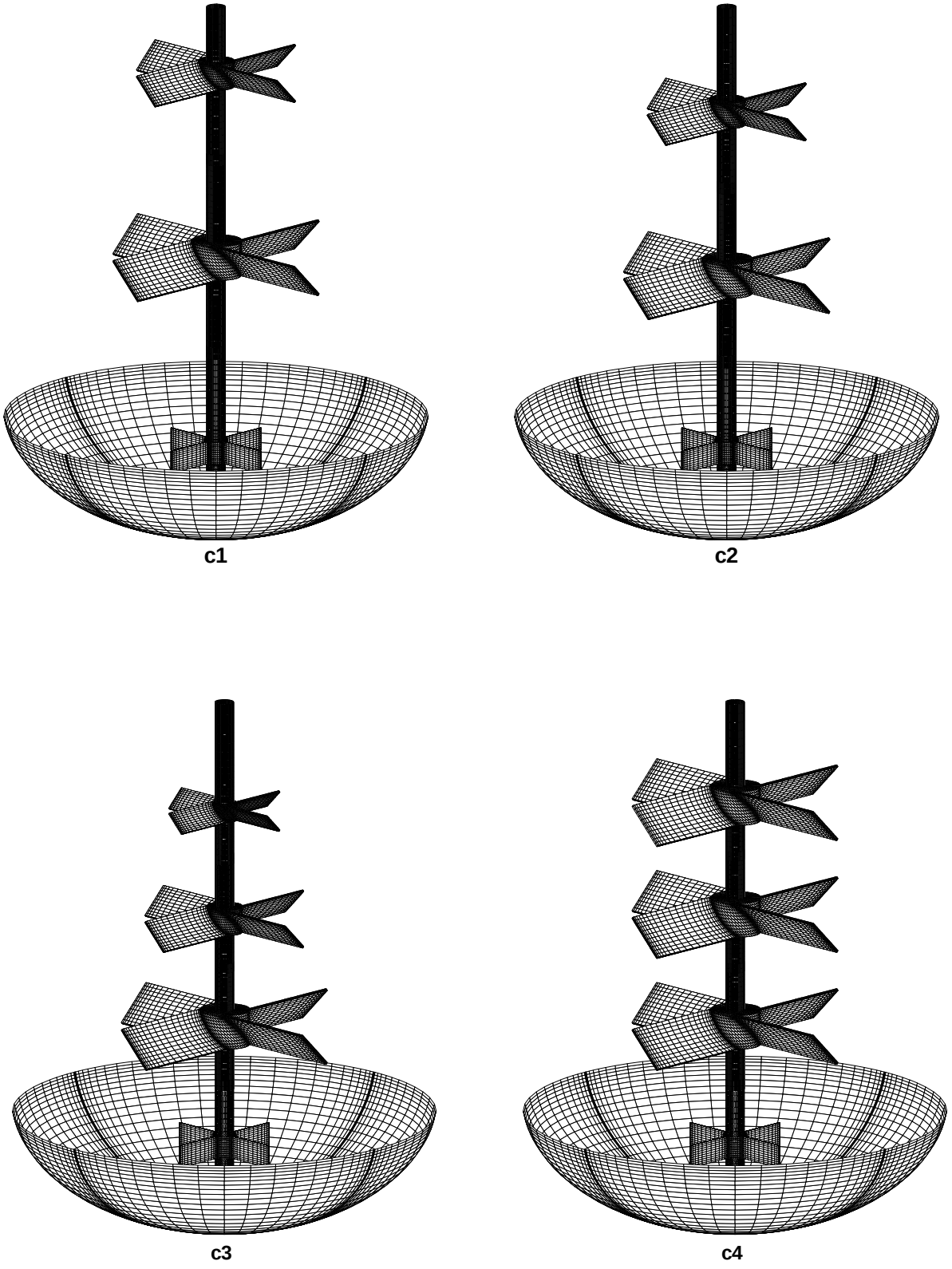

Fig. 3: Geometry and surface grid for cases 1–4.

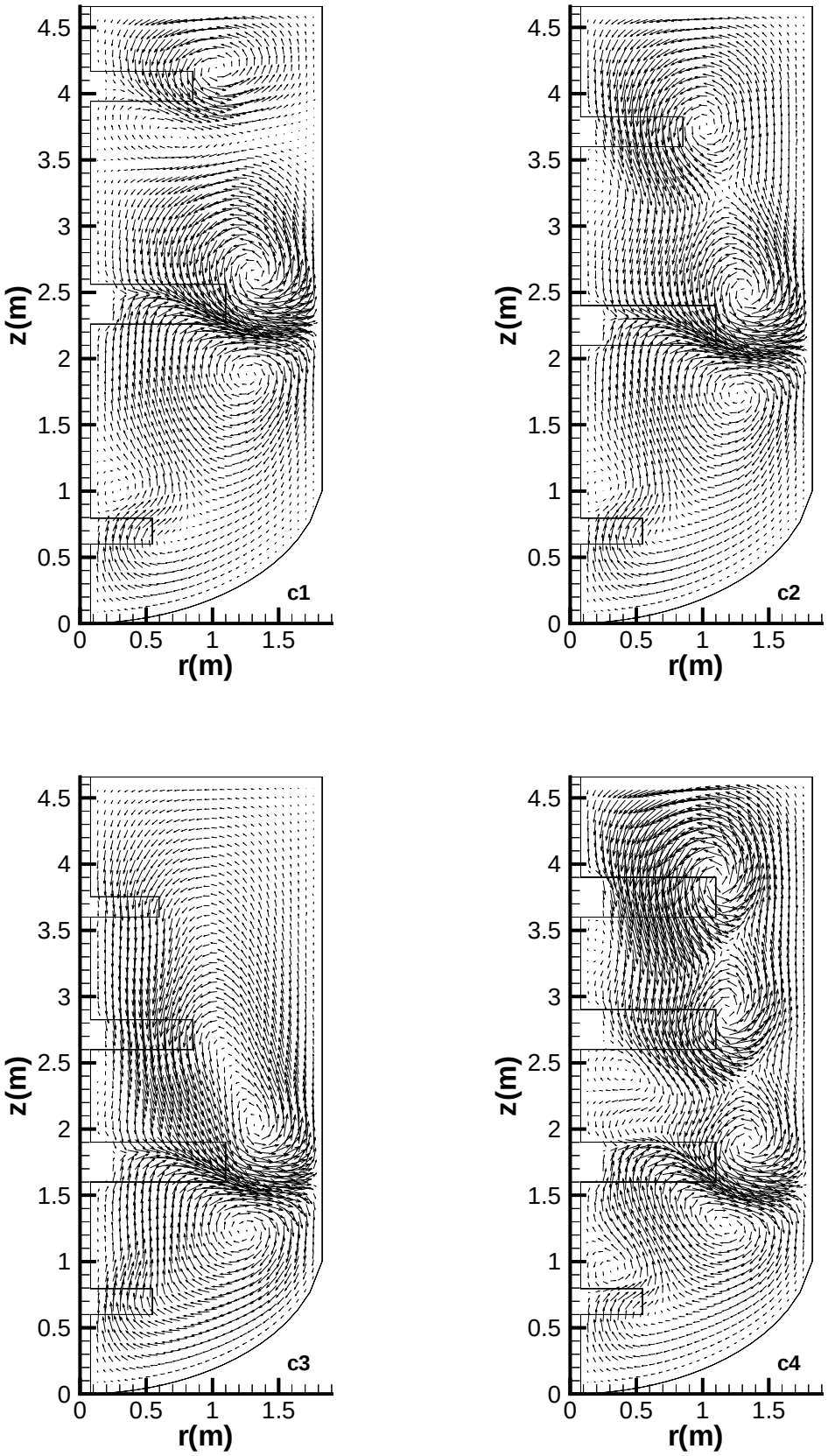

Fig. 4*a–d*: Time-averaged velocity vectors for cases 1–4.

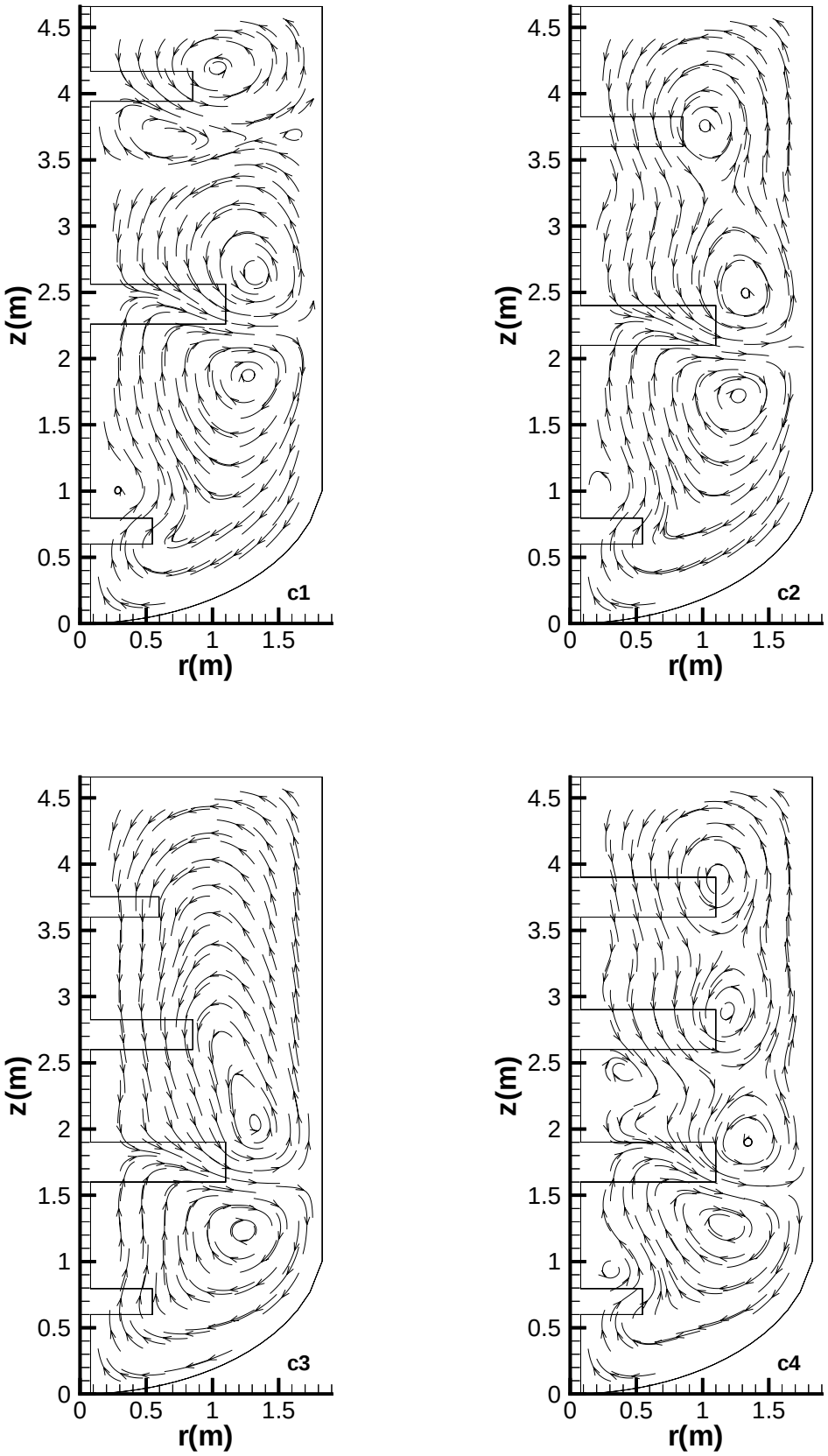

Fig. 5*a–d*: Cross-flow streamlines for cases 1–4.

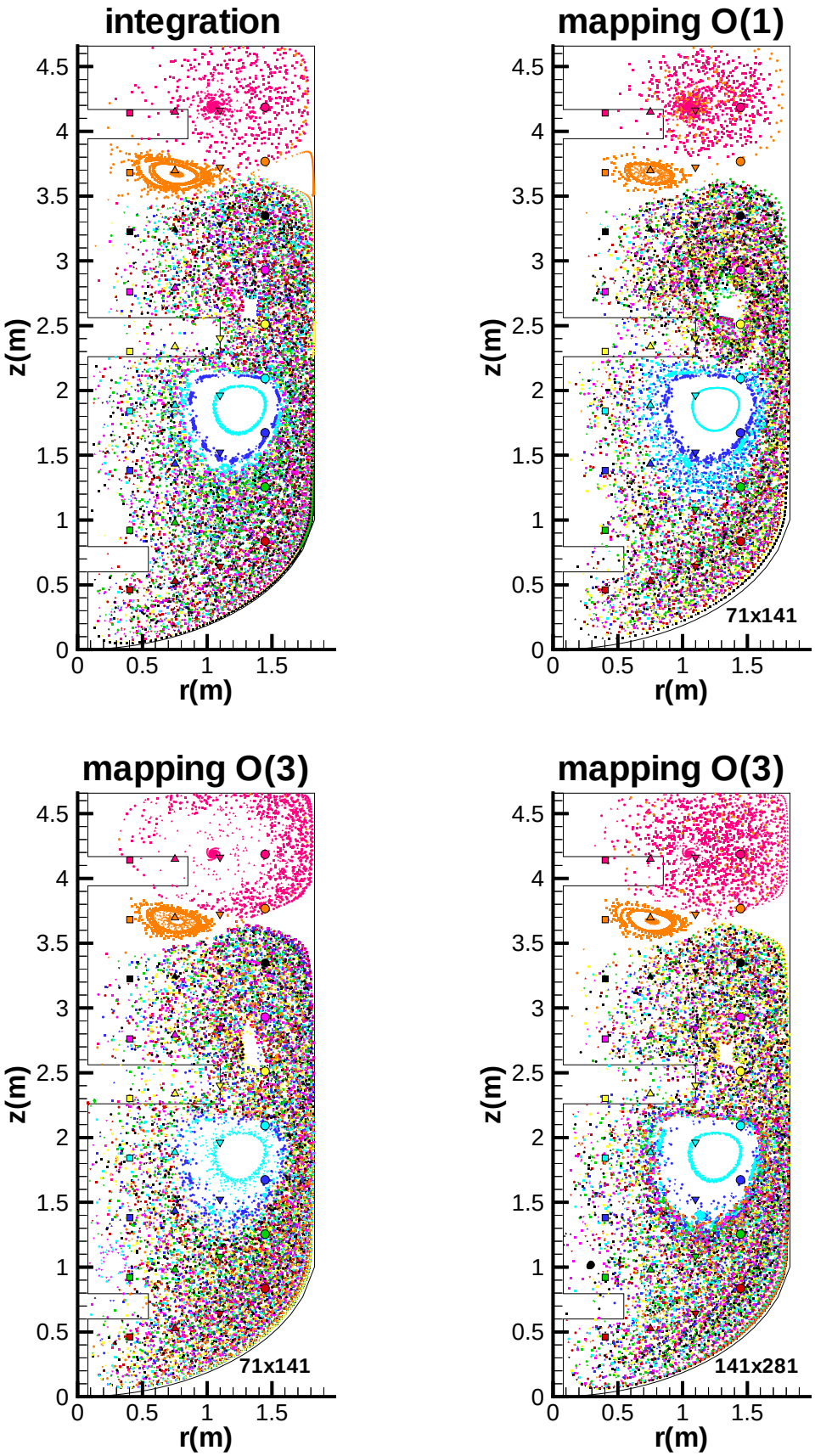

Fig. 6*a–d*: Poincaré maps for case 1. (*a*) Integration; (*b*) coarse grid, bi-linear mapping interpolation; (*c*) coarse grid, bi-cubic interpolation; (*d*) fine grid, bi-cubic interpolation.

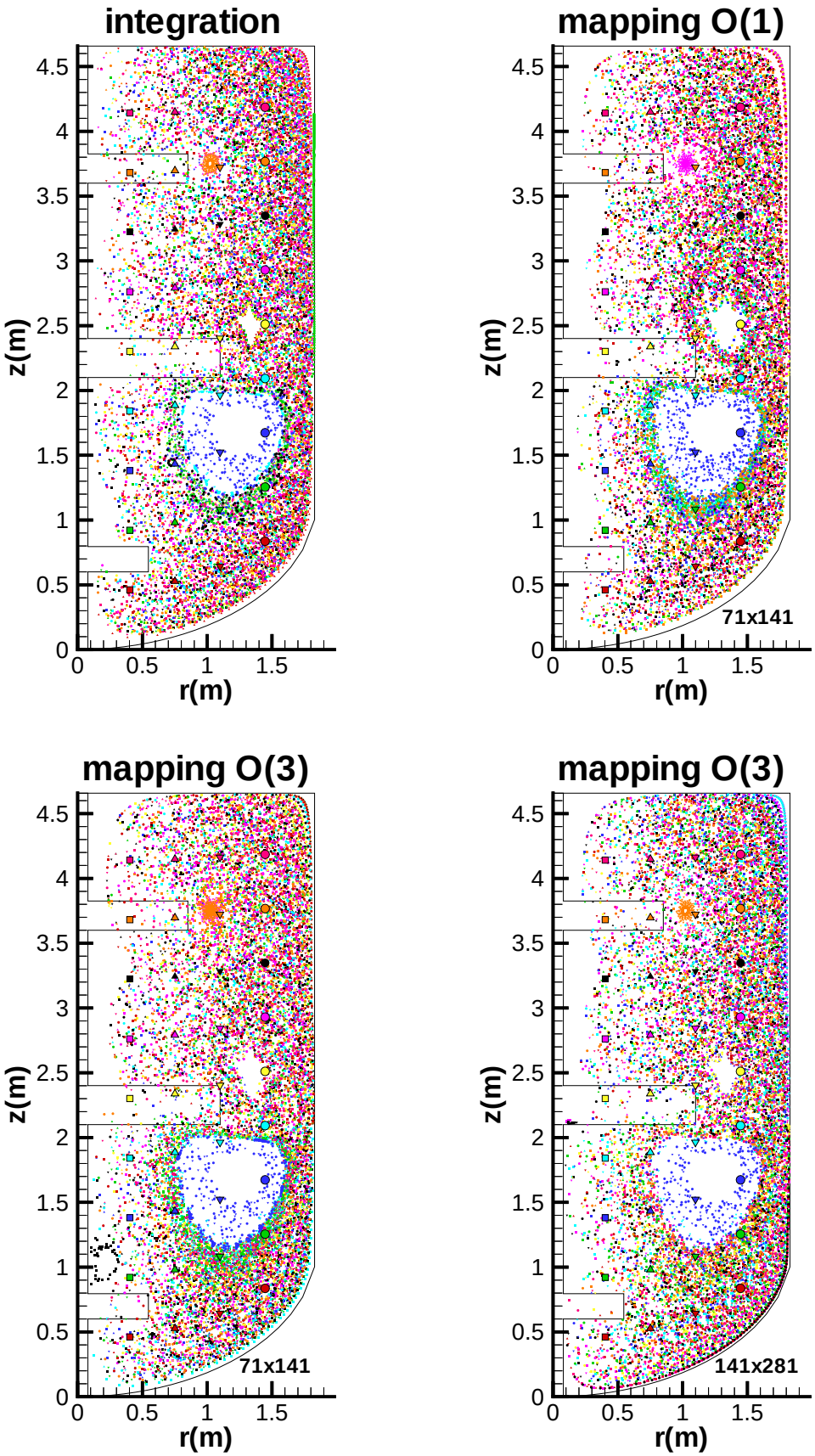

Fig. 7*a–d*: Poincaré maps for case 2. (*a*) Integration; (*b*) coarse grid, bi-linear mapping interpolation; (*c*) coarse grid, bi-cubic interpolation; (*d*) fine grid, bi-cubic interpolation.

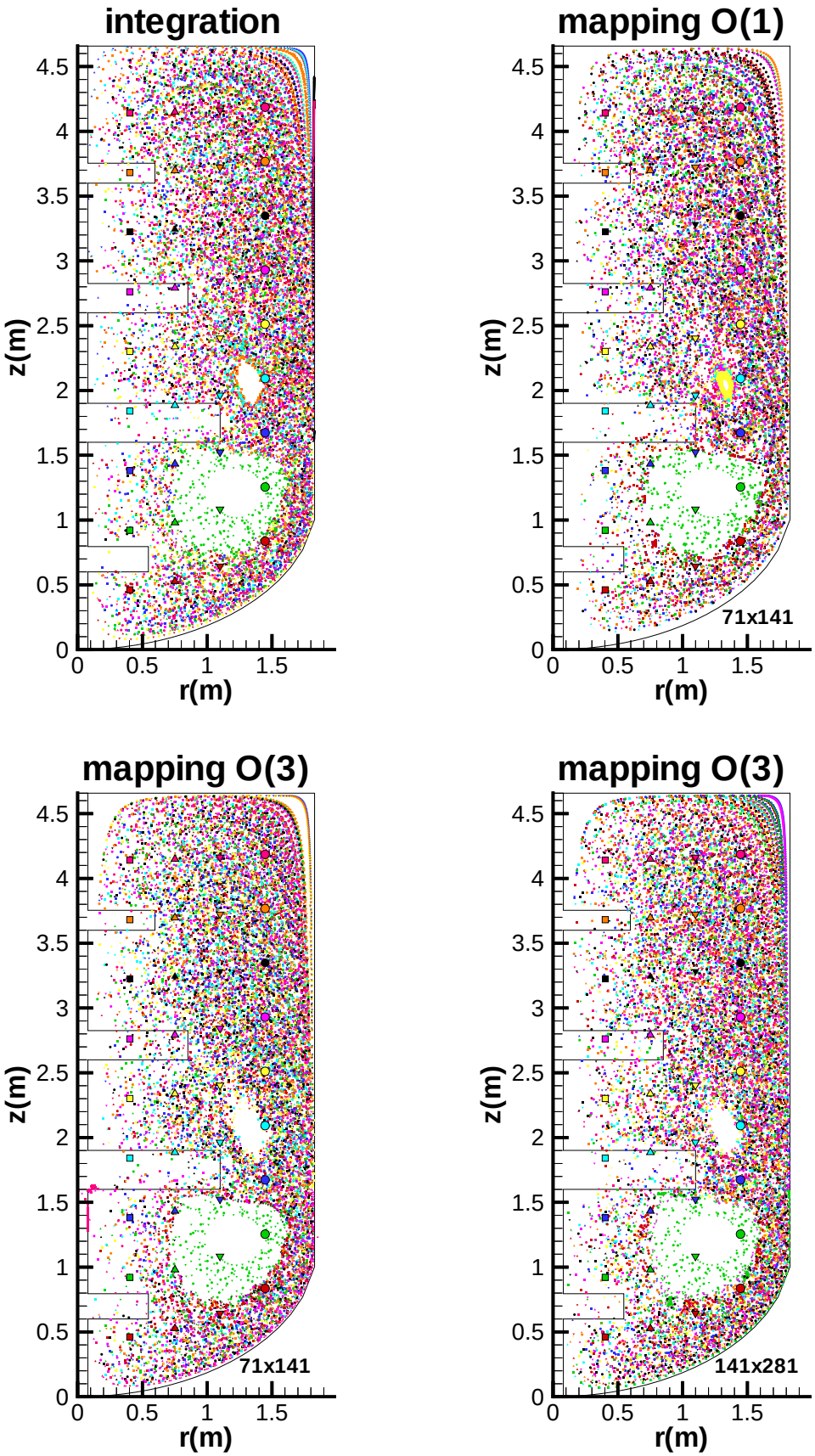

Fig. 8*a–d*: Poincaré maps for case 3. (*a*) Integration; (*b*) coarse grid, bi-linear mapping interpolation; (*c*) coarse grid, bi-cubic interpolation; (*d*) fine grid, bi-cubic interpolation.

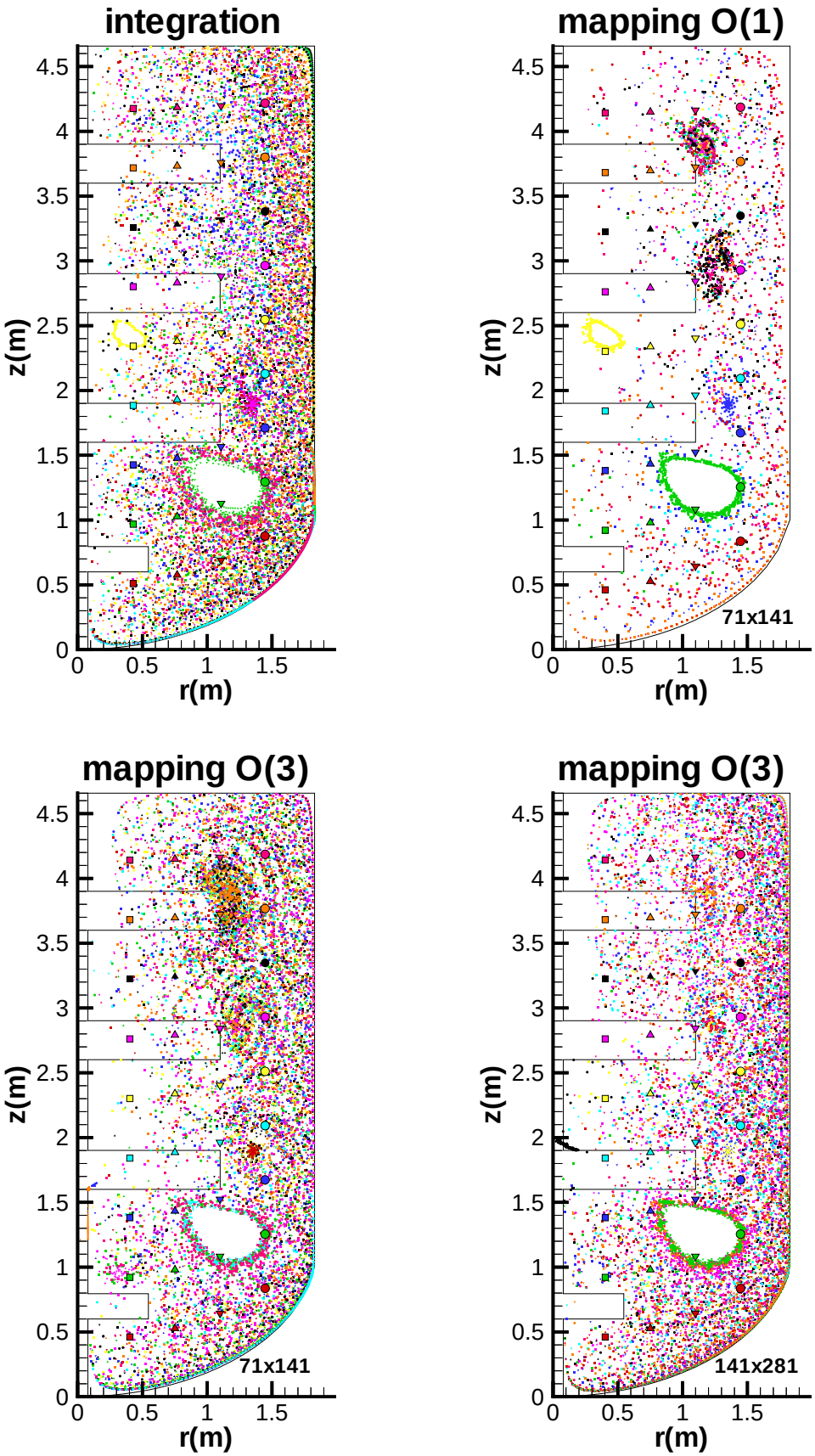

Fig. 9*a–d*: Poincaré maps for case 4. (*a*) Integration; (*b*) coarse grid, bi-linear mapping interpolation; (*c*) coarse grid, bi-cubic interpolation; (*d*) fine grid, bi-cubic interpolation.

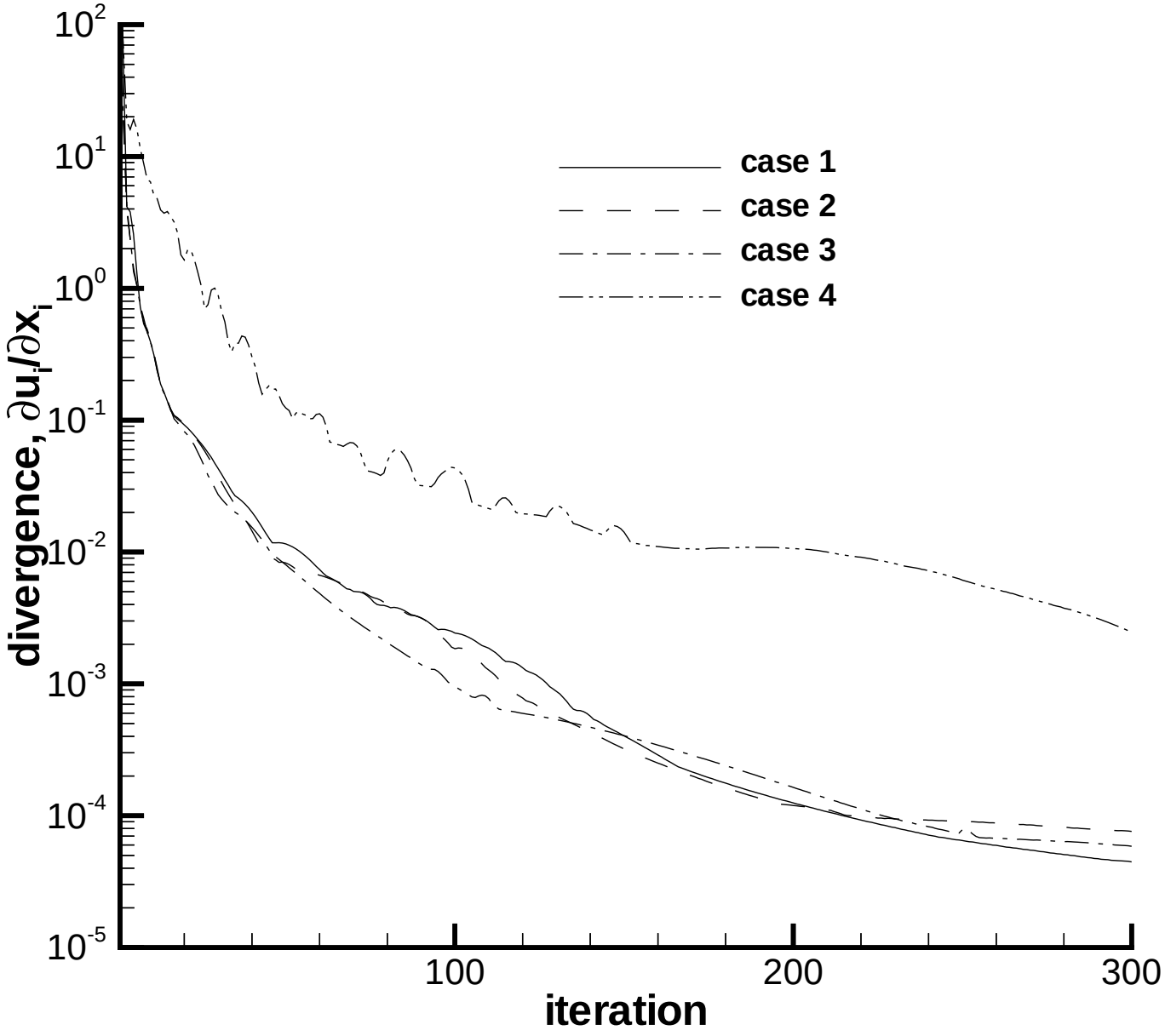

Fig. 10: Plot of the history of the divergence of the velocity field for the CFD calculations (cases 1–4).

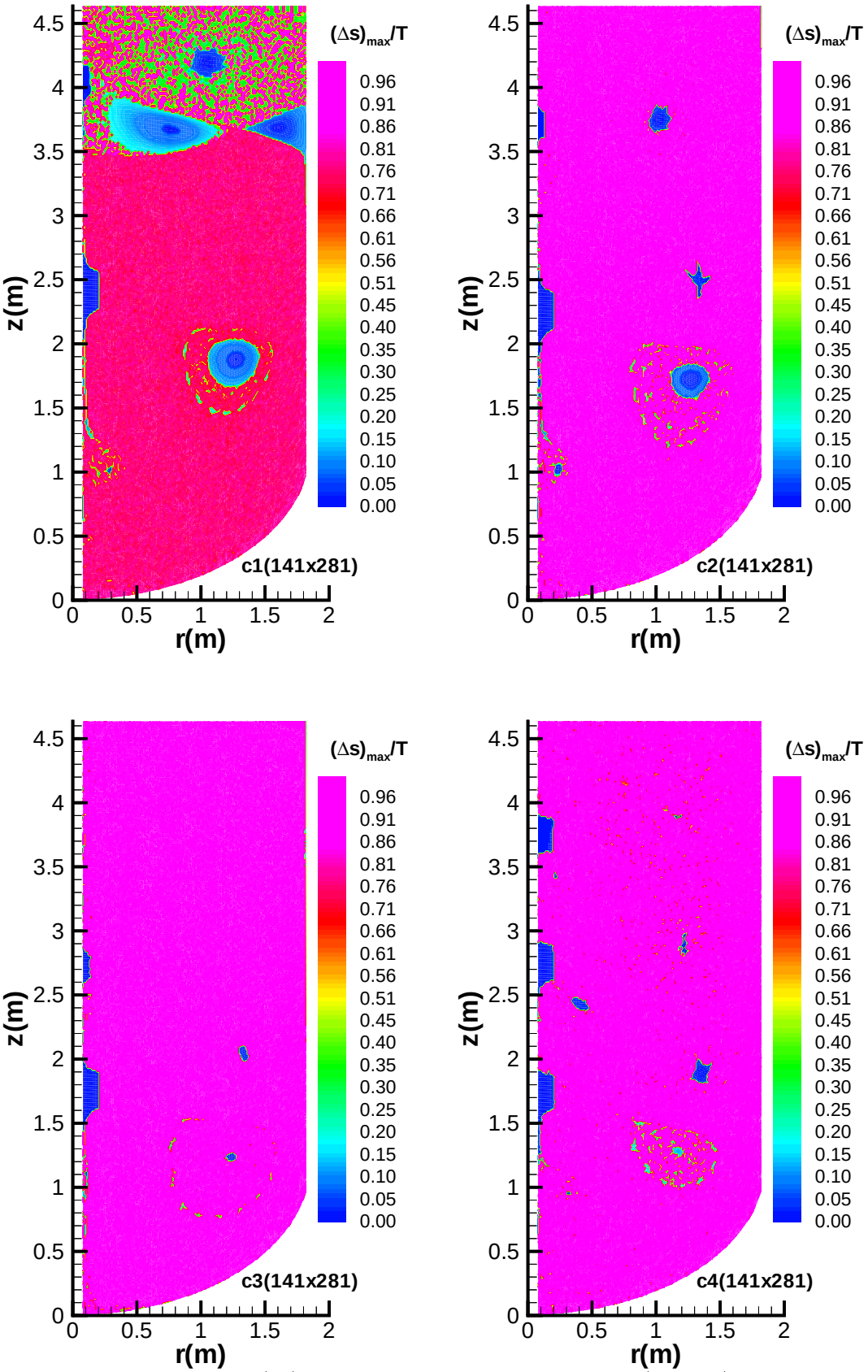

Fig. 11*a–d*: $(\Delta s)_{max}$ as a function of position in the vessel (cases 1–4).

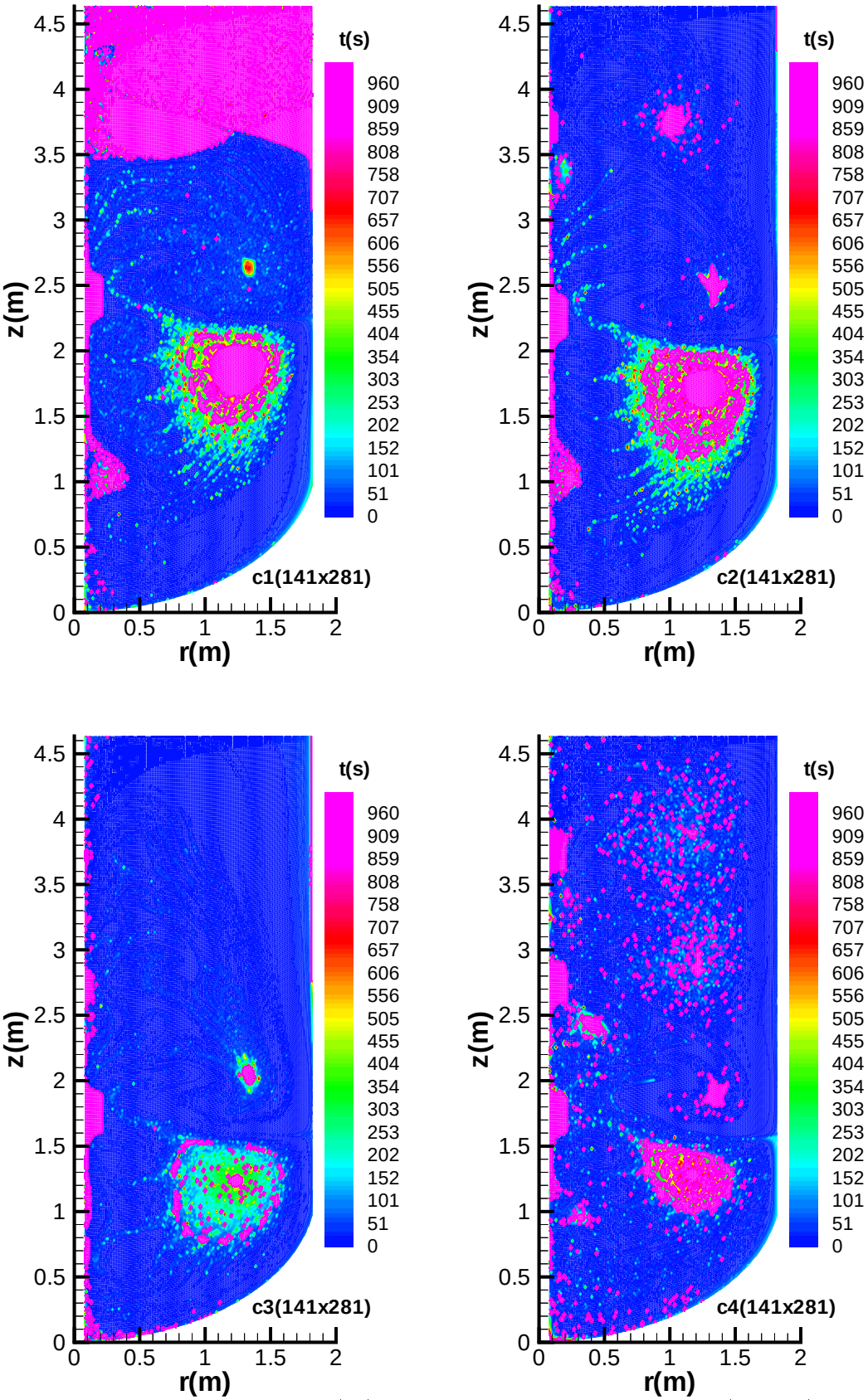

Fig. 12*a–d*: Time to achieve $(\Delta s)_{max}$ as a function of position in the vessel (cases 1–4).

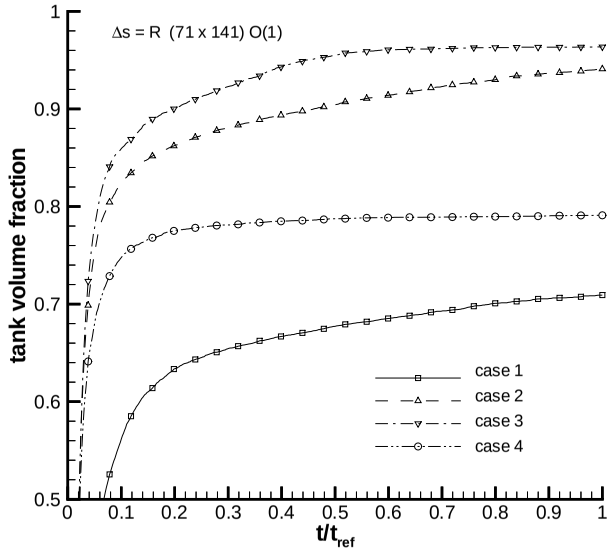

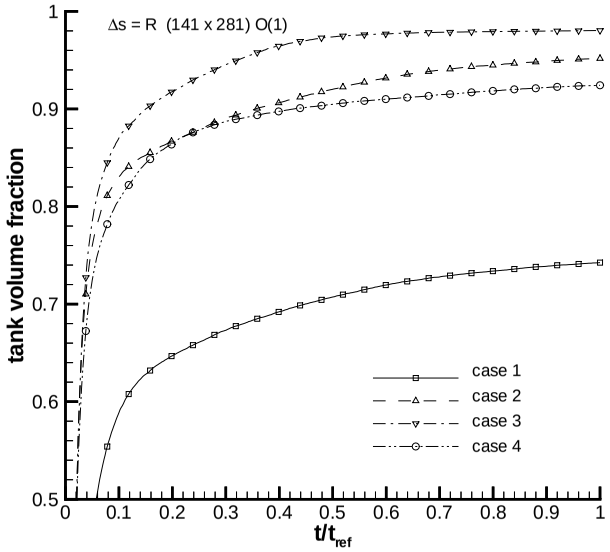

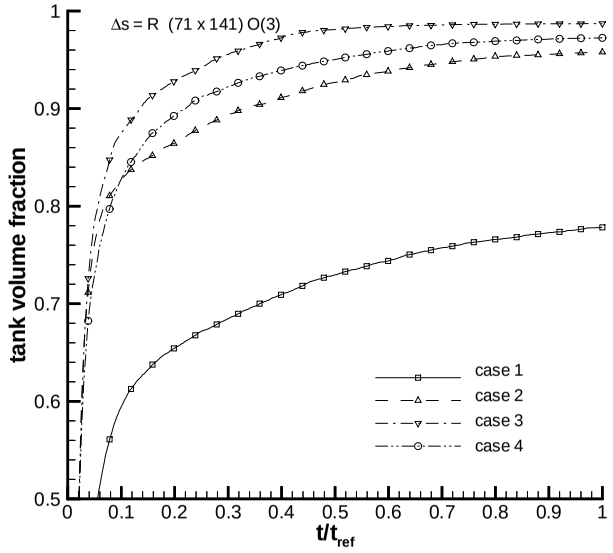

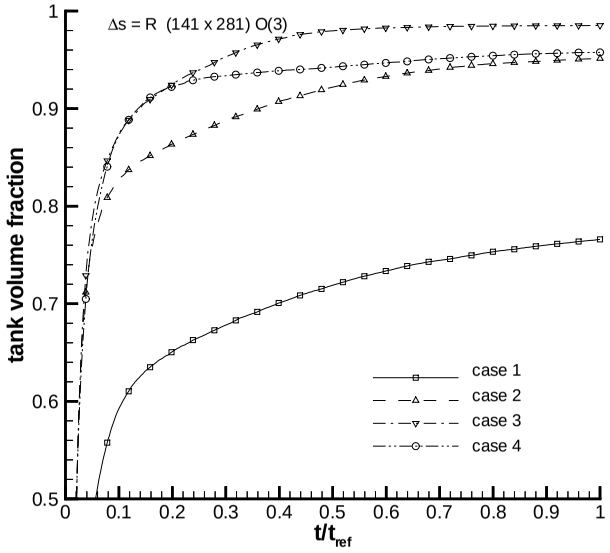

Fig. 13*a–d*: Tank volume fraction with $\Delta s \geq (\Delta s)_{max}$ vs. time for the 4 different mappings.